Important Impact of the Slurry Mixing Speed on Water-Processed $Li_4Ti_5O_{12}$ Lithium-Ion Anodes in the Presence of H_3PO_4 as the Processing Additive

Yun Xu, Shan Fang, Maider Zarrabeitia, Matthias Kuenzel, Dorin Geiger, Ute Kaiser, Stefano Passerini, and Dominic Bresser*

ABSTRACT: The aqueous processing of lithium transition metal oxides into battery electrodes is attracting a lot of attention as it would allow for avoiding the use of harmful *N*-methyl-2-pyrrolidone (NMP) from the cell fabrication process and, thus, render it more sustainable. The addition of slurry additives, for instance phosphoric acid (PA), has been proven to be highly effective for overcoming the corresponding challenges such as aluminum current collector corrosion and stabilization of the active material particle. Herein, a comprehensive investigation of the effect of the ball-milling speed on the effectiveness of PA as a slurry additive is reported using $Li_4Ti_5O_{12}$ (LTO) as an exemplary lithium transition metal oxide. Interestingly, at elevated ball-milling speeds, rod-shaped lithium phosphate particles are formed, which remain absent at lower ball-milling speeds. A detailed surface characterization by means of SEM, EDX, HRTEM, STEM-EDX, XPS, and EIS revealed that in the latter case, a thin protective phosphate layer is formed on the LTO particles, leading to an improved electrochemical performance. As a result, the corresponding lithium-ion cells comprising LTO anodes and $LiNi_{0.5}Mn_{0.3}Co_{0.2}O_2$ (NMC_{532}) cathodes reveal greater long-term cycling stability and higher capacity retention after more than 800 cycles. This superior performance originates from the less resistive electrode−electrolyte interphase evolving upon cycling, owing to the interface-stabilizing effect of the lithium phosphate coating formed during electrode preparation. The results highlight the importance of commonly neglected—frequently not even reported—electrode preparation parameters.

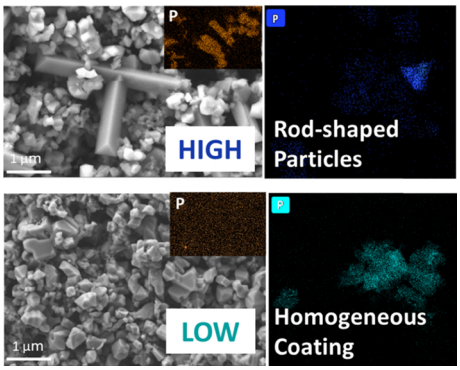

KEYWORDS: *$Li_4Ti_5O_{12}$, Li_3PO_4, aqueous processing, anode, lithium-ion battery*

1. INTRODUCTION

Lithium-ion batteries (LIBs) are employed as energy storage technology of choice for a wide range of applications, including small-scale devices such as laptops and mobile phones, electric vehicles (hybrid), and large-scale stationary storage.[1−6] This tremendous success originates from their outstanding performance and the worldwide target to reduce the emission of greenhouse gases. In this regard, though, it is of great importance that the technology itself is also sustainable, which includes the materials and components used as well as the battery fabrication and the transition to purely water-based electrode preparation processes.[7−9] An additional benefit of the latter, besides the replacement of harmful organic solvents and fluorine-comprising polymers as binders, is the facilitated recycling and potential recovery of the active materials from spent cells.[10] While it has been well implemented already for graphite-based electrodes, the high reactivity of lithium transition metal oxides such as $LiNi_{1-x-y}Mn_xCo_yO_2$ (NMC), $LiNi_{0.5}Mn_{1.5}O_4$ (LNMO), and $Li_4Ti_5O_{12}$ (LTO) renders the aqueous processing challenging.[9] This is of particular importance for high-safety and high-power LIBs,[11−13] which are solely composed of lithium transition metal oxides, that is, LTO‖NMC_{111},[14] LTO‖Li-rich NMC,[15] and LTO‖LNMO.[16,17] The contact with water results in a rapid increase of the slurry pH value owing to Li^+ leaching and hydroxide formation, which induces the corrosion of the aluminum current collector.[9,18] Additionally, the accordingly modified surface of the active material particles favors side reactions with the electrolyte upon cycling and, thus, leads to reduced cycle life and capacity retention.[19,20] Generally, the addition of carefully selected acids, such as PA, has been reported as an effective measure to buffer the pH value, suppress aluminum corrosion, and stabilize the active material surface by forming a

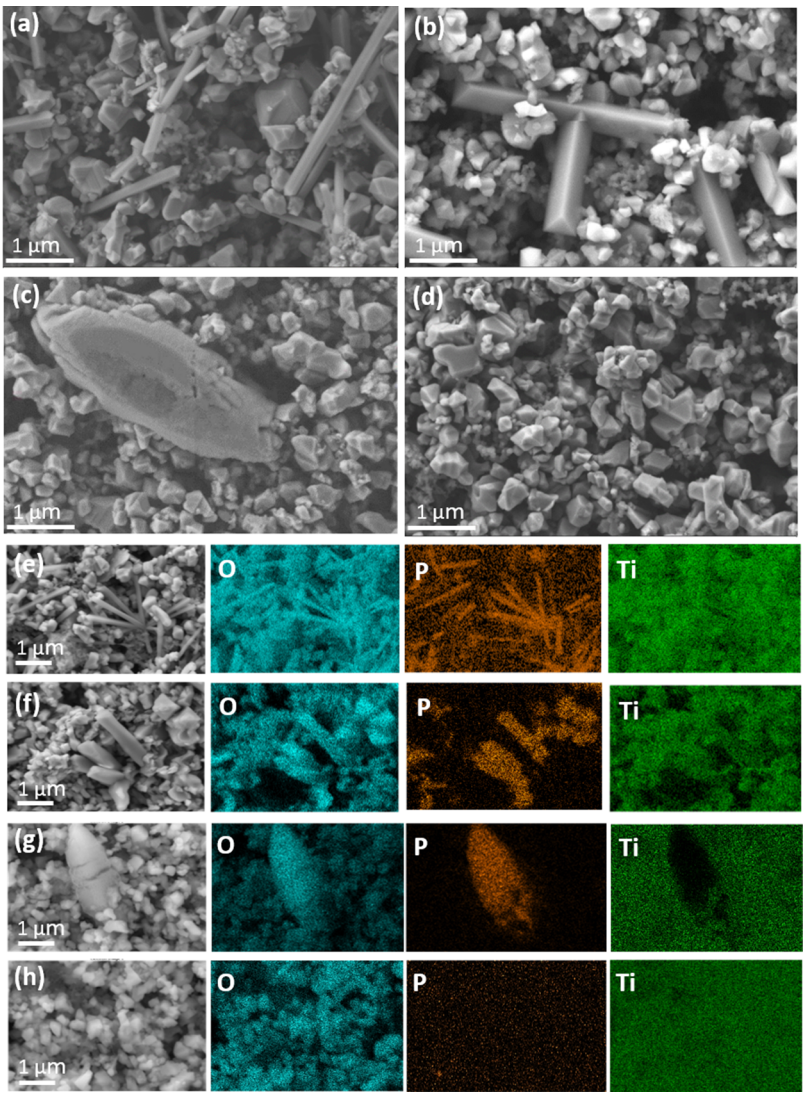

Figure 1. (a–d) SEM micrographs of pristine LTO electrodes, for which different ball-milling speeds were used for the slurry dispersion: (a) 1260 rpm, (b) 1100 rpm, (c) 1000 rpm, and (d) 900 rpm. (e–h) SEM–EDX analysis of these electrodes with an elemental mapping of oxygen, phosphorus, and titanium (from left to right): (e) 1260 rpm, (f) 1100 rpm, (g) 1000 rpm, and (h) 900 rpm.

thin metal phosphate layer.[21−23] Very recently, however, we have found that, in the case of LTO, the addition of PA leads to the formation of rod-shaped lithium (titanium) phosphate particles rather than a homogeneous coating layer.[24]

Herein, we report a comprehensive investigation of the impact of the ball-milling speed as a decisive parameter for the formation of such rod-shaped particles—or, in contrast, the formation of a homogeneous lithium phosphate coating on the LTO particle surface. The latter turns out to be advantageous for the long-term cycling stability of LTO||Li half-cells and LTO||NMC_{532} full-cells as it stabilizes the electrode–electrolyte interface more effectively and enables a lower charge transfer resistance upon cycling.

2. EXPERIMENTAL SECTION

2.1. Materials and Electrode Preparation. Commercially available LTO (NEI Corporation, average particle size: 1.5–3.0 μm) was used as-received. C-NERGY Super C45 (Imerys) was used as a conductive additive, and sodium carboxymethyl cellulose (CMC, Dow Wolff Cellulosics, Walocel CRT 2000; degree of substitution: 1.2) was utilized as a binder. PA (>99%, Bernd Kraft; 33% in aqueous solution) was employed as a slurry additive to buffer the pH of the slurry. The LTO-based electrodes were prepared as follows: CMC was dissolved in deionized water by magnetic stirring at room temperature. The thus-obtained solution, PA (2.68 wt % of the amount of LTO, as optimized in a previous study[24]), LTO, and the conductive carbon were transferred into zirconia ball mill grinding jars with an inner diameter of around 40 mm and a height of 60 mm. Overall, the solid content was about 28% (2.6 g of water and 1.0 g of solid material). The slurry was ball-milled for 2 h at different milling speeds, as indicated in the main text. The milling was performed using two different sizes of zirconia grinding balls, that is, 2 bigger ones with a diameter of ca. 10 mm and 17 smaller ones with a diameter of about 5 mm. The ball-milled slurry was cast on a battery grade aluminum foil using a laboratory-scale doctor blade. Subsequently, the electrodes were dried in an atmospheric oven (Binder) at 80 °C, before being transferred to the dry room. Disk-shaped electrodes with a geometric area of 1.13 cm^2 were cut and pressed at 5 t for 10 s (Atlas manual hydraulic press, Specac). Finally, the electrodes were dried again under vacuum at 120 °C for 12 h. The active material mass loading of the electrodes was in the range from 5.6 to 5.8 mg cm^{-2}. The overall composition of the electrodes was 88 wt % LTO, 5 wt % conductive carbon, and 7 wt % CMC in all experiments shown herein; only when varying the binder content, we changed the electrode composition to 88 wt % LTO, 7 wt % conductive carbon, and 5 wt % CMC or 88 wt % LTO, 9 wt % conductive carbon, and 3 wt % CMC (see Figure S1).

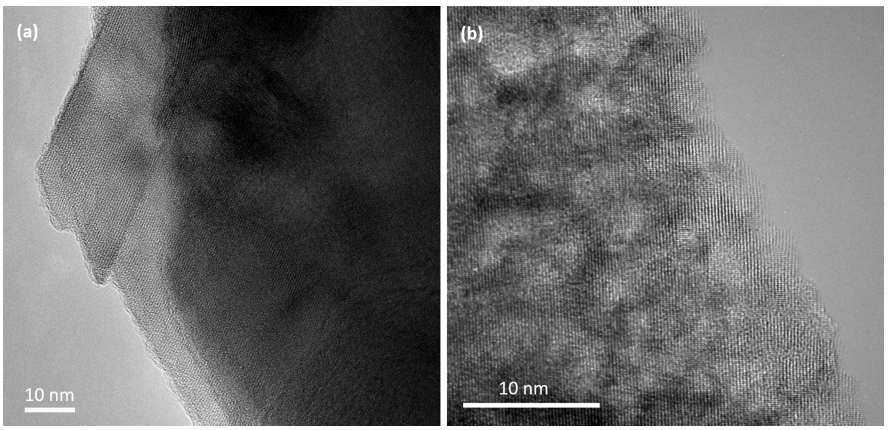

Figure 2. HRTEM micrographs of the pristine LTO electrodes subjected to a milling speed of (a) 900 rpm and (b) 1100 rpm, i.e., electrodes for which the formation of rod-shaped lithium (titanium) phosphate was absent and present, respectively.

2.2. Physicochemical Characterization. Scanning electron microscopy (SEM) was performed on a Zeiss Crossbeam 340 field-emission electron microscope, which is equipped with an energy-dispersive X-ray (EDX) spectrometer (Oxford Instruments X-Max Xtreme, 100 mm^2, 1−5 kV). X-ray photoelectron spectroscopy (XPS) was conducted using a Phoibos 150 XPS spectrometer equipped with a microchannel plate, a delay line detector (DLD), and a monochromatic Al K_α ($h\nu$ = 1486.6 eV) X-ray source. High-resolution scans were acquired with an X-ray source power of 200 W, a pass energy of 20 eV, and energy steps of 0.1 eV in a fixed analyzer transmission mode. The cells were disassembled in the glovebox after 10 cycles for the ex situ XPS analysis on cycled electrodes. The recovered electrodes were rinsed with dimethyl carbonate (DMC) prior to the transfer into the XPS load lock vacuum chamber via an argon-filled transfer vessel to avoid any contact with air and moisture. The XPS data were calibrated using the graphitic carbon (C═C) peak from the conductive additive at 284.4 eV as the reference. The fitting of the spectra was carried out with the CasaXPS software using a nonlinear Shirley-type background and a 70% Gaussian and 30% Lorentzian profile function, except for the hydrocarbons (C−C/C−H), for which an asymmetric line shape was used. High-resolution transmission electron microscopy (HRTEM) was performed using a TEM FEI Titan 80−300 kV with an image C_s-corrector, operated at an accelerating voltage of 300 kV. Scanning TEM (STEM) coupled with an EDX analysis was conducted on a TEM Thermofisher Talos 200X with a dedicated SuperX EDX detector, operated at an accelerating voltage of 200 kV. X-ray diffraction (XRD) was carried out using a Bruker D8 Advance diffractometer with Cu K_α radiation (λ = 0.15406 nm). The XRD patterns were recorded in the 2θ range from 5° to 70° with a step size of 0.008° (2θ) and an acquisition time of 1 s/point.

2.3. Electrochemical Characterization. Three-electrode Swagelok-type T-cells with lithium-metal foil (battery grade, Honjo) as counter and reference electrodes and LTO as the working electrode were used for the electrochemical characterization in half-cells. The cell assembly was performed in an argon-filled glovebox (MBraun) with a H_2O and O_2 content lower than 0.1 ppm. Glass fiber disks (Whatman GF/D) were used as a separator and soaked with 120 μL of the electrolyte solution (1 M $LiPF_6$ in ethylene carbonate (EC)/dimethyl carbonate (DMC), 1:1 w/w, UBE). For the galvanostatic cycling, a Maccor Battery Tester 4300 was used, and the cut-off potentials were set to 2.5 and 1.0 V vs Li^+/Li (T = 20 ± 2 °C). An applied discharge/charge rate of 1C corresponds to a specific current of 175 mA g^{-1} and a current density of about 1.0 mA cm^{-2}. Electrochemical impedance spectroscopy (EIS) was performed on a multichannel potentiostat (VMP3, BioLogic). The impedance spectra were recorded in three-electrode ECC-PAT-Core cells (EL-CELL) utilizing a circular lithium-metal ring as the quasi-reference electrode and lithium-metal foil disks as counter electrodes. The AC voltage amplitude was 5 mV, and the frequency range was 1 MHz to 10 mHz. Additionally, selected LTO-based electrodes were tested in LTO||NMC_{532} full-cells. These full-cells were tested in coin cells and cycled in a voltage range from 1.4 to 2.7 V. The positive electrode was composed of 92 wt % NMC_{532} (BASF), 4 wt % Super C65 (Imerys), and 4 wt % PVdF (Solef 6020, Solvay), coated on aluminum foil (battery grade). The capacity ratio of the negative and positive electrodes, that is, the N/P ratio, was about 1.14 in all cases. For these full-cells, a discharge/charge rate of 1C corresponds to a specific current of 161 mA g^{-1} and a current density of around 0.9 mA cm^{-2}.

3. RESULTS AND DISCUSSION

To evaluate the impact of the ball-milling speed on the LTO-based electrodes, SEM was performed. The SEM images presented in Figure 1a−d correspond to the electrodes obtained by mixing the electrode slurry at 1260, 1100, 1000, and 900 rpm, respectively. At the maximum milling speed of 1260 rpm (Figure 1a), elongated rods are observed with a length of several micrometers and a thickness of about 0.2 μm. Our previous work has shown that these rods are composed of lithium (titanium) phosphate, which are formed during the electrode preparation in the presence of PA.[24] When decreasing the milling speed to 1100 rpm, these rods become slightly shorter, still several micrometers, though, and slightly thicker of about 0.5 μm (Figure 1b). Further decreasing the milling speed to 1000 rpm leads to the formation of even thicker rods with a thickness of about 1.3 μm and a comparably irregular shape (Figure 1c). Interestingly, a similar observation was made when varying the CMC content in the electrode slurry subjected to 1100 rpm, revealing thicker rods for higher CMC contents (Figure S1). This suggests that the viscosity of the slurry is affected by the CMC content[25] and/or the milling speed, in turn playing a decisive role on the diffusion of the leached cations and the growth of these rod-shaped particles. Most remarkably, however, is the disappearance of such rod-shaped particles when reducing the milling speed to only 900 rpm (Figure 1d). In this case, only particles with the initial morphology of the LTO particles are observed (see Figure S2 for comparison). The subsequently performed elemental mapping via EDX spectroscopy (Figure 1e−h) confirms that the rod-shaped particles are composed of oxygen and phosphorus and partially also titanium, revealing the formation of lithium phosphate and lithium titanium phosphate particles.[24] Differently, the elemental distribution of the three elements is very homogeneous across the whole sampled electrode for a milling speed of 900 rpm (Figure 1h),

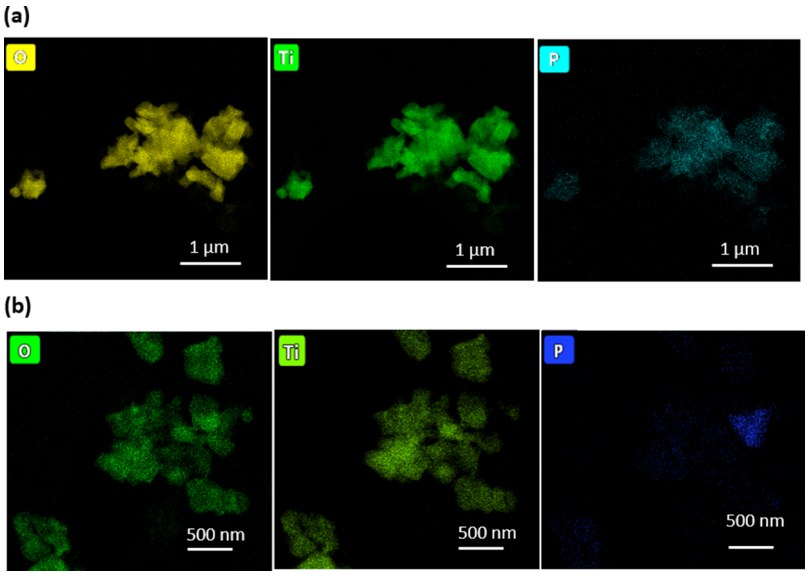

Figure 3. STEM-EDX mapping of oxygen, titanium, and phosphorus (from left to right) for LTO samples subjected to a milling speed of (a) 900 rpm and (b) 1100 rpm, i.e., the "rod-free" and a "rod-containing" sample, respectively.

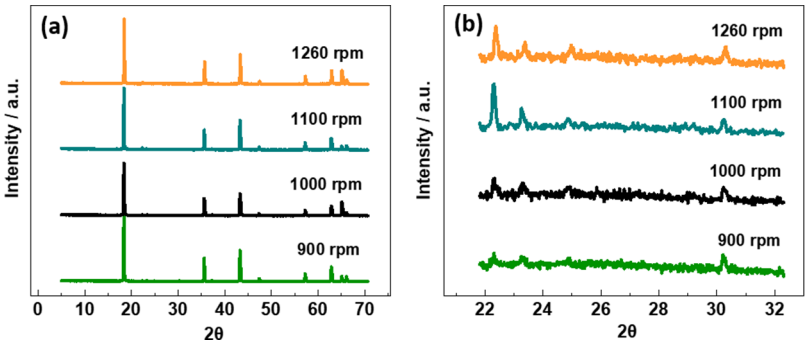

Figure 4. (a) XRD patterns of the pristine LTO electrodes subjected to different milling speeds during the electrode preparation, i.e., 1260, 1100, 1000, and 900 rpm (from top to bottom). (b) Magnification of the 2θ region between 22° and 32°.

suggesting the formation of a lithium (titanium) phosphate coating layer on the LTO particles.

The formation of such a surface layer was confirmed by HRTEM, which reveals a thin amorphous layer on top of the LTO particles with a generally very smooth (crystalline) particle surface beyond this coating layer (Figure 2a). Differently, the HRTEM micrograph of the sample subjected to a milling speed of 1100 rpm, serving as an example for the electrodes for which the formation of rod-shaped particles was observed, does not show such a surface layer but generally a very rough and edgy particle surface (Figure 2b). These findings suggest that the presence of the lithium (titanium) phosphate coating on the LTO particles stabilizes the surface and prevents excessive reaction with the acidic water. The formation of a homogeneous coating layer in the case of the "rod-free" sample was further corroborated by STEM coupled with EDX mapping, revealing an even distribution of oxygen, titanium, and phosphorus across all the particles on the corresponding images (Figure 3a). In contrast, the STEM-EDX analysis of the "rod-containing" sample shows a single phosphorus-containing particle, in which titanium is essentially absent (Figure 3b). This particle has a triangular shape rather than the characteristic rod shape, suggesting that this is a fraction of a rod-shaped particle—which, in fact, has a triangular shape as well (Figure 1b).

In the next step, the four samples were characterized by XRD (Figure 4). At the first view, the XRD patterns recorded for the different electrodes appear very similar (Figure 4a). However, significant differences are observed when magnifying the 2θ region between 20° and 35° (Figure 4b). All patterns reveal the formation of a new phase with reflections at about 22.3° and 23.3°, which has been earlier assigned to Li_3PO_4.[24] These reflections are relatively intense, though, for the samples that have been subjected to elevated milling speeds of 1260 and 1100 rpm, while they become less intense for the sample subjected to 1000 rpm and even less for the one subjected to a milling speed of 900 rpm. This finding is in line with the very crystalline appearance of the rods in the former two cases (Figure 1a,b) and the less crystalline appearance in the case of 1000 rpm (Figure 1c) and their absence in the case of 900 rpm (Figure 1d). These findings indicate that higher ball-milling speeds are favorable for the crystal growth of Li_3PO_4. Moreover, the observation of Li_3PO_4-related reflections in the case of 900 rpm shows that the coating layer on the LTO particles is not fully amorphous but partially crystalline.

For the following electrochemical characterization, we focused on the comparison of the rod-free electrodes (i.e., 900 rpm) and exemplarily for the rod-containing electrodes on the sample subjected to the medium milling speed of 1100 rpm. The comparison of the galvanostatic cycling is presented

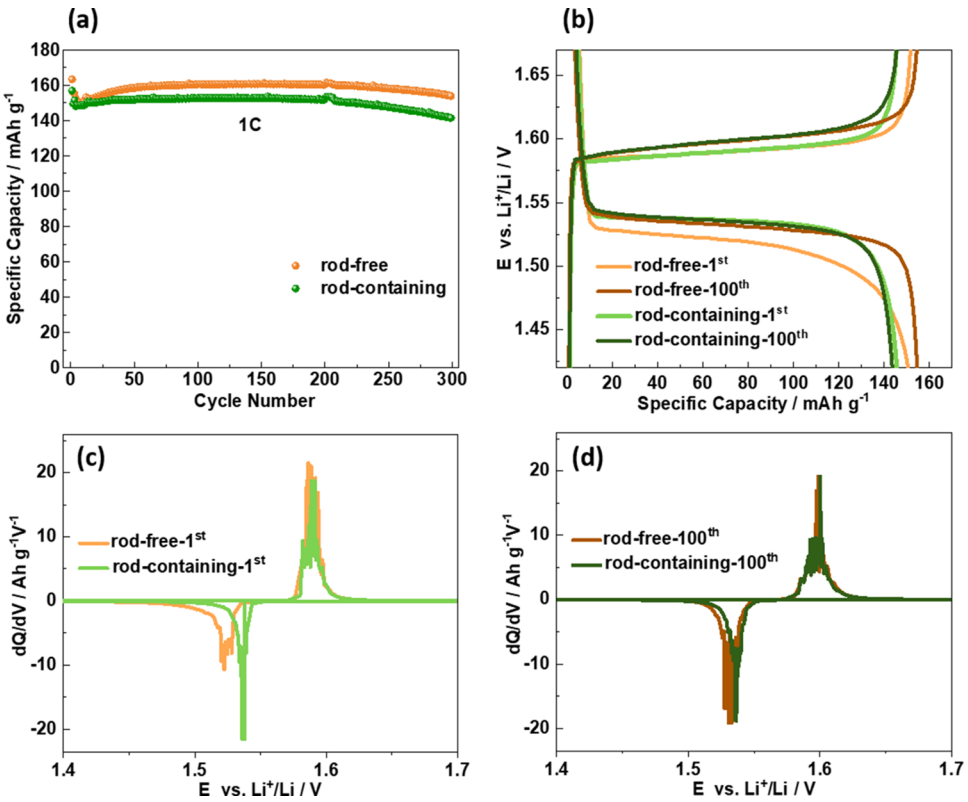

Figure 5. Galvanostatic cycling of rod-free (in orange) and rod-containing (in green) LTO electrodes at 1C (cut-off potentials: 1.0 and 2.5 V vs Li^+/Li): (a) plot of the specific discharge capacity vs the cycle number; (b) comparison of the discharge/charge profiles of the 1st and 100th cycles; and (c,d) plots of the differential capacity of the two electrodes for the (c) 1st and (d) 100th cycles.

in Figure 5a. The initial specific discharge (lithiation) capacity of the rod-free and the rod-containing electrodes at 1C is 163 and 157 mAh g^{-1}, respectively. After 300 cycles at 1C, the rod-free electrodes provide a specific discharge capacity of 154 mAh g^{-1}, which corresponds to a capacity retention of 94.5% compared to the first cycle at 1C. For the rod-containing electrode, a specific discharge capacity of 141 mAh g^{-1} was recorded, which corresponds to a somewhat lower capacity retention of 89.8%. Accordingly, the presence of the lithium (titanium) phosphate coating layer is beneficial for the cycling stability, presumably by suppressing side reactions with the electrolyte, as indicated also by the slightly higher Coulombic efficiency (Figure S4), and for the achievable capacity in general. This is assigned to the stabilized LTO surface, as observed by HRTEM (Figure 2), revealing the preservation of the initially smooth particle surface. Differently, in the case of the rod-containing electrodes, the roughened surface is expected to provide a slightly decreased amount of available sites for the Li^+ insertion. Besides, it appears noteworthy that the capacity is slightly increasing upon cycling for the rod-free electrodes. This increase originates from a decreasing polarization upon discharge, as apparent from the comparison of the discharge/charge profiles for the 1st and 100th cycles in Figure 5b and the comparison of the differential capacity plots for these two cycles in Figure 5c and Figure 5d, respectively, while it remains essentially constant for the rod-containing electrodes. This decrease in polarization for the lithiation step in the case of the rod-free electrodes is assigned to an initially higher energy barrier for the Li^+ cations to enter the LTO particles through the lithium phosphate layer. This layer might get more conductive upon repeated cycling. In fact, the pristine lithium phosphate layer is (in part) lithium-deficient (see also the discussion of the XPS data in the following) and might get enriched in lithium upon cycling. As a matter of fact, the Li^+ conductivity of Li_3PO_4 is generally rather high (10^{-6} to 10^{-8} S cm^{-1})[26] compared to that of LTO (10^{-13} S cm^{-1}).[27] These results are generally in good agreement with previous studies on, for instance, Li_3PO_4-coated LTO,[27] $LiMn_2O_4$,[28] and $LiNi_{0.8}Co_{0.15}Al_{0.05}O_2$[29]—all showing enhanced cycling stability owing to the application of such coating.

The observations concerning the polarization are also well reflected by the EIS data recorded after the 1st (Figure 6a) and 100th (Figure 6b) cycles. While the impedance is initially higher for the cell comprising the rod-free LTO electrode, it decreases to a comparable value as the one recorded for the cell with the rod-containing LTO electrode upon continuous

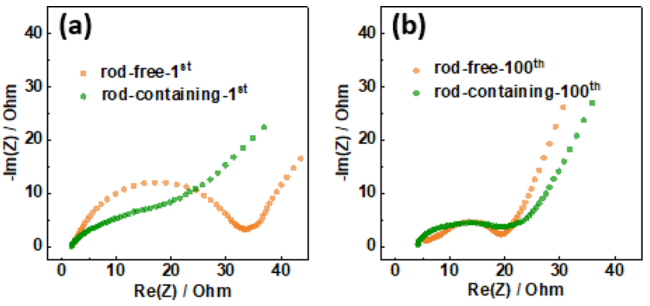

Figure 6. Comparison of the EIS data recorded for the cells comprising the rod-free LTO electrodes (in orange) and the rod-containing electrodes (in green) at the discharged state (i.e., at 1.0 V) after the (a) 1st and (b) 100th cycles.

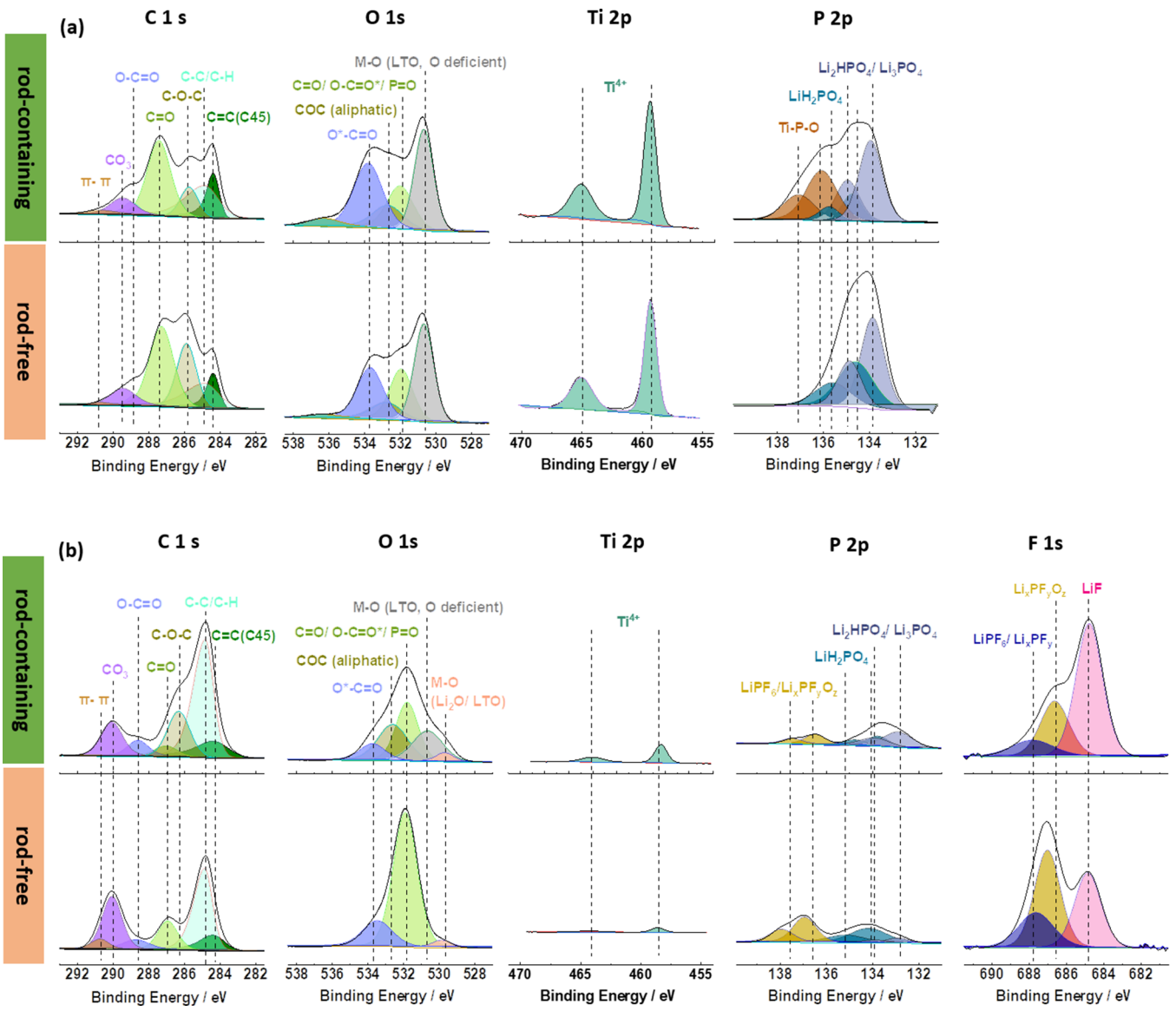

Figure 7. XPS analysis of (a) pristine and (b) cycled rod-containing (top) and rod-free (bottom) LTO electrodes. The cycled electrodes were recovered after 10 discharge/charge cycles in half-cells.

cycling, which is in line with the evolution of the polarization depicted in Figure 5c,d.

To better understand the differences between the two samples, an ex situ XPS analysis was conducted for cycled rod-free and rod-containing LTO electrodes, and the results were compared with the XPS data recorded for the pristine electrodes (Figure 7). The C 1s spectra of both pristine electrodes (Figure 7a) reveal peaks that were assigned to C═C (284.4 eV) and $\pi-\pi$ (290.7 eV) bonds from the conductive carbon, as well as C−C/C−H (284.8 eV), C−O−C (285.9 eV), C═O (287.3 eV), and O═C−O (288.8 eV) from the sodium CMC binder.[30] Additionally, a relatively minor peak at 289.4 eV was assigned to carbonate (CO_3) species, presumably resulting from the exposure of the pristine LTO electrodes to the ambient atmosphere (see also the H_2O-related peak at 536.3 eV in the O 1s spectra of the pristine electrodes, originating from water adsorption). The cycled electrodes (Figure 7b) show a reduced intensity of the C═C (conductive carbon)- and C═O (CMC binder)-related peaks, indicating the formation of the solid electrolyte interphase (SEI) layer. Meanwhile, the relative intensity of the CO_3, O═C−O, and C−C/C−H peaks increased after cycling because of the electrolyte solvent decomposition. In comparison, the cycled rod-containing LTO electrode shows a higher concentration of C−C/C−H, C−O−C, and O═C−O species. In contrast, the rod-free electrode presents a higher amount of carbonate species, suggesting that the SEI on the rod-containing electrode contains a larger fraction of organic species (such as oligo-/polyethers resulting from the ring-opening reaction of EC[31]), while the SEI on the rod-free electrode contains more inorganic species such as lithium carbonate (see also the elemental composition in Figure S5). These results suggest a different route for the EC and DMC decomposition in the two cases as a consequence of the lithium phosphate coating in the case of the rod-free LTO electrodes.[32] In fact, a greater contribution of inorganic species such as lithium carbonate was reported to be advantageous for the cycling stability.[33] The analysis of the O 1s region shows a similar picture to that observed for the C 1s region with a relatively greater intensity of the C−O−C (532.8 eV)-related peak, that is, organic

species, while the rod-free electrodes reveal a greater intensity of the peak attributed to C═O/O═C−O*/P═O (531.9 eV)[22,34] (with a rather large contribution of P═O species presumably, as indicated in the P 2p and F 1s spectra). Generally, the M−O peak (529.8 eV) and the peak at 530.7 eV, assigned to oxygen-deficient LTO,[35,36] substantially decreased in intensity, further corroborating the formation of an SEI on the LTO surface. In fact, the latter completely disappeared for the rod-free electrodes after cycling, indicating a slightly thicker and/or less X-ray permeable SEI in this case, as evident also from the comparison of the Ti 2p spectra.[37] The P 2p spectra of the pristine electrodes reveal rather intense peaks attributed to H_3PO_4/LiH_2PO_4 (P $2p_{3/2}$: 134.6 eV) and Li_2HPO_4/Li_3PO_4 (P $2p_{3/2}$: 133.8 eV),[36] which is in line with our previous study[24] and the XRD data presented in Figure 4. Remarkably, the peak observed at 136.1 eV (P $2p_{3/2}$) for the pristine rod-containing LTO electrodes, which is assigned to Ti−P−O and suggests the presence of a lithium titanium phosphate phase, is absent for the pristine rod-free LTO electrodes. This finding indicates that the presence of a sufficient amount of dissolved titanium cations in the slurry might play a role in the formation of the rod-shaped particles. For both kinds of electrodes, though, the signal intensity of the cycled electrodes is substantially reduced owing to the formation of the SEI. The latter appears to contain a larger fraction of $LiPF_6$ decomposition products, however, in the case of the rod-free electrodes, as indicated by the higher intensity of the $LiPF_6/Li_xPF_yO_z$-related peak (P $2p_{3/2}$: 136.9 eV).[22,38] This observation is in good agreement with the F 1s spectra of the cycled electrodes, also showing a greater intensity of the $Li_xPF_yO_z$ peak at 687.0 eV and the $LiPF_6/Li_xPF_y$-related peak at 687.6 eV[38] compared to the rod-containing electrodes. In the latter case, the F 1s spectrum is largely dominated by a more intense LiF (684.8 eV) peak[39] than for the rod-free electrodes.

In sum, the presence of the lithium phosphate coating layer on the LTO particles has a significant effect on the electrolyte decomposition and SEI formation, yielding a thicker and/or less X-ray permeable interphase that is more inorganic in nature compared to the SEI formed on the rod-containing LTO electrodes. Simultaneously, the presence of the lithium phosphate coating leads to the formation of less LiF, while "less decomposed" reaction products such as Li_xPF_y and $Li_xPF_yO_z$ dominate. With regard to the beneficial effect of electrolyte additives such as $LiPO_2F_2$[40] and the earlier discussed advantageous impact of a more inorganic SEI in general, these findings may explain the better capacity retention observed in Figure 5a.

To further corroborate this conclusion, LTO‖NMC_{532} full-cells were assembled with the two different LTO electrodes and subjected to long-term galvanostatic cycling (Figures 8 and S6). Both cells reveal a very comparable and, generally, very stable cycling behavior for the depicted 800 cycles. The initial specific capacity at 0.1C is about 150 mAh g^{-1} (referring to the active material mass of the NMC_{532}-positive electrode) in both cases, which decreases to 126 mAh g^{-1} when the discharge/charge rate is increased to 1C. Nonetheless, the capacity retention is slightly higher after 800 cycles at 1C for the full-cells comprising the rod-free LTO electrodes with 96.8% (i.e., 122 mAh g^{-1}) compared to the full-cells comprising the rod-containing LTO electrodes with 91.3% (i.e., 115 mAh g^{-1}). This superior capacity retention and cycling stability further highlight the beneficial impact of the lithium phosphate coating compared to the simple presence of such separated particles; which in turn highlights the importance of carefully controlling the electrode preparation parameters when introducing reactive processing additives such as PA.

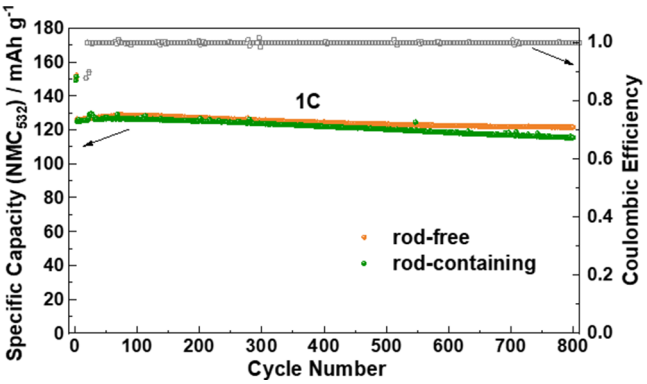

Figure 8. Long-term galvanostatic cycling of LTO‖NMC_{532} full-cells, comprising rod-free LTO electrodes (in orange) and rod-containing LTO electrodes (in green). Following two formation cycles at 0.1C, the cells were cycled at a discharge/charge rate of 1C for 800 cycles. The cut-off voltages were set to 1.4 and 2.7 V.

4. CONCLUSIONS

The milling speed plays an important role when adding PA as a highly effective processing additive to aqueous $Li_4Ti_5O_{12}$ (LTO) electrode slurries. At elevated milling speeds, rod-shaped particles are formed that are composed of lithium (titanium) phosphate, while at lower milling speeds, a thin lithium phosphate coating is formed on the LTO particles. The in situ realization of such coating during the electrode preparation combines the general beneficial effects of PA, including the buffered pH value and the suppression of aluminum current collector corrosion, with a stabilized electrodelelectrolyte interface and SEI, owing to a greater contribution of inorganic species in the SEI. Therefore, the capacity retention in half-cells and LTO‖NMC_{532} full-cells was improved—in the latter case, from about 91 to almost 97% after 800 cycles at 1C. These results highlight the importance of a comprehensive understanding of the reactions occurring in aqueous electrode slurries for lithium transition metal oxide active materials in the presence of "reactive" processing additives and the potential manifold benefits when carefully designing the processing parameters.

■ ASSOCIATED CONTENT

● Supporting Information

The Supporting Information is available free of charge at https://pubs.acs.org/doi/10.1021/acsami.2c10744.

SEM micrographs of the as-received LTO powder and LTO electrodes comprising varying amounts of binder; galvanostatic cycling at varying C rates; Coulombic efficiency plots for half-cells and LTO‖NMC_{532} full-cells; and quantification of the XPS data obtained for cycled electrodes (PDF)

■ AUTHOR INFORMATION

Corresponding Author

Dominic Bresser − *Helmholtz Institute Ulm (HIU), 89081 Ulm, Germany; Karlsruhe Institute of Technology (KIT),*

76021 Karlsruhe, Germany; orcid.org/0000-0001-6429-6048; Email: dominic.bresser@kit.edu

Authors

Yun Xu − *Helmholtz Institute Ulm (HIU), 89081 Ulm, Germany; Karlsruhe Institute of Technology (KIT), 76021 Karlsruhe, Germany*

Shan Fang − *Helmholtz Institute Ulm (HIU), 89081 Ulm, Germany; Karlsruhe Institute of Technology (KIT), 76021 Karlsruhe, Germany;* orcid.org/0000-0001-9497-994X

Maider Zarrabeitia − *Helmholtz Institute Ulm (HIU), 89081 Ulm, Germany; Karlsruhe Institute of Technology (KIT), 76021 Karlsruhe, Germany*

Matthias Kuenzel − *Helmholtz Institute Ulm (HIU), 89081 Ulm, Germany; Karlsruhe Institute of Technology (KIT), 76021 Karlsruhe, Germany;* orcid.org/0000-0002-5877-7053

Dorin Geiger − *Central Facility for Electron Microscopy, Ulm University, 89081 Ulm, Germany*

Ute Kaiser − *Central Facility for Electron Microscopy, Ulm University, 89081 Ulm, Germany*

Stefano Passerini − *Helmholtz Institute Ulm (HIU), 89081 Ulm, Germany; Karlsruhe Institute of Technology (KIT), 76021 Karlsruhe, Germany;* orcid.org/0000-0002-6606-5304

Complete contact information is available at: https://pubs.acs.org/10.1021/acsami.2c10744

Notes

The authors declare no competing financial interest.

■ ACKNOWLEDGMENTS

Y.X. would like to acknowledge financial support from the Chinese Scholarship Council (CSC). Moreover, the authors would like to thank the Helmholtz Association and the German Federal Ministry of Education and Research for financial support within the ExcellBattUlm project (03XP0257D).

■ REFERENCES

(1) Armand, M.; Tarascon, J.-M. Building Better Batteries. *Nature* **2008**, *451*, 652−657.

(2) Belharouak, I.; Koenig, G. M.; Tan, T.; Yumoto, H.; Ota, N.; Amine, K. Performance Degradation and Gassing of $Li_4Ti_5O_{12}$/$LiMn_2O_4$ Lithium-Ion Cells. *J. Electrochem. Soc.* **2012**, *159*, A1165−A1170.

(3) Dunn, B.; Kamath, H.; Tarascon, J.-M. Electrical Energy Storage for the Grid: A Battery of Choices. *Science* **2011**, *334*, 928−935.

(4) Bresser, D.; Hosoi, K.; Howell, D.; Li, H.; Zeisel, H.; Amine, K.; Passerini, S. Perspectives of Automotive Battery R&D in China, Germany, Japan, and the USA. *J. Power Sources* **2018**, *382*, 176−178.

(5) Armand, M.; Axmann, P.; Bresser, D.; Copley, M.; Edström, K.; Ekberg, C.; Guyomard, D.; Lestriez, B.; Novák, P.; Petranikova, M.; Porcher, W.; Trabesinger, S.; Wohlfahrt-Mehrens, M.; Zhang, H. Lithium-Ion Batteries − Current State of the Art and Anticipated Developments. *J. Power Sources* **2020**, *479*, No. 228708.

(6) Marinaro, M.; Bresser, D.; Beyer, E.; Faguy, P.; Hosoi, K.; Li, H.; Sakovica, J.; Amine, K.; Wohlfahrt-Mehrens, M.; Passerini, S. Bringing Forward the Development of Battery Cells for Automotive Applications: Perspective of R&D Activities in China, Japan, the EU and the USA. *J. Power Sources* **2020**, *459*, No. 228073.

(7) Larcher, D.; Tarascon, J.-M. Towards Greener and More Sustainable Batteries for Electrical Energy Storage. *Nat. Chem.* **2015**, *7*, 19−29.

(8) Wood, D. L.; Quass, J. D.; Li, J.; Ahmed, S.; Ventola, D.; Daniel, C. Technical and Economic Analysis of Solvent-Based Lithium-Ion Electrode Drying with Water and NMP. *Drying Technol.* **2017**, 1−11.

(9) Bresser, D.; Buchholz, D.; Moretti, A.; Varzi, A.; Passerini, S. Alternative Binders for Sustainable Electrochemical Energy Storage − The Transition to Aqueous Electrode Processing and Bio-Derived Polymers. *Energy Environ. Sci.* **2018**, *11*, 3096−3127.

(10) Li, J.; Lu, Y.; Yang, T.; Ge, D.; Wood, D. L.; Li, Z. Water-Based Electrode Manufacturing and Direct Recycling of Lithium-Ion Battery Electrodes—A Green and Sustainable Manufacturing System. *iScience* **2020**, *23*, No. 101081.

(11) Han, X.; Ouyang, M.; Lu, L.; Li, J. Cycle Life of Commercial Lithium-Ion Batteries with Lithium Titanium Oxide Anodes in Electric Vehicles. *Energies* **2014**, *7*, 4895−4909.

(12) Cicconi, P.; Postacchini, L.; Pallotta, E.; Monteriú, A.; Prist, M.; Bevilacqua, M.; Germani, M. A Life Cycle Costing of Compacted Lithium Titanium Oxide Batteries for Industrial Applications. *J. Power Sources* **2019**, *436*, No. 226837.

(13) Wu, K.; Yang, J.; Zhang, Y.; Wang, C.; Wang, D. Investigation on $Li_4Ti_5O_{12}$ Batteries Developed for Hybrid Electric Vehicle. *J. Appl. Electrochem.* **2012**, *42*, 989−995.

(14) Farhat, D.; Ghamouss, F.; Maibach, J.; Edström, K.; Lemordant, D. Adiponitrile−Lithium Bis(Trimethylsulfonyl)Imide Solutions as Alkyl Carbonate-Free Electrolytes for $Li_4Ti_5O_{12}$ (LTO)/$LiNi_{1/3}Co_{1/3}Mn_{1/3}O_2$ (NMC) Li-Ion Batteries. *ChemPhysChem* **2017**, *18*, 1333−1344.

(15) Dai, C.; Ye, J.; Zhao, S.; He, P.; Zhou, H. Fabrication of High-Energy Li-Ion Cells with $Li_4Ti_5O_{12}$ Microspheres as Anode and $0.5Li_2MnO_3{\cdot}0.5LiNi_{0.4}Co_{0.2}Mn_{0.4}O_2$ Microspheres as Cathode. *Chem. − Asian J.* **2016**, *11*, 1273−1280.

(16) Zheng, J.; Xiao, J.; Nie, Z.; Zhang, J.-G. Lattice Mn^{3+} Behaviors in $Li_4Ti_5O_{12}$/$LiNi_{0.5}Mn_{1.5}O_4$ Full Cells. *J. Electrochem. Soc.* **2013**, *160*, A1264−A1268.

(17) Kuenzel, M.; Kim, G.-T.; Zarrabeitia, M.; Lin, S. D.; Schuer, A. R.; Geiger, D.; Kaiser, U.; Bresser, D.; Passerini, S. Crystal Engineering of TMPOx-Coated $LiNi_{0.5}Mn_{1.5}O_4$ Cathodes for High-Performance Lithium-Ion Batteries. *Mater. Today* **2020**, *39*, 127−136.

(18) Hawley, W. B.; Parejiya, A.; Bai, Y.; Meyer, H. M.; Wood, D. L.; Li, J. Lithium and Transition Metal Dissolution Due to Aqueous Processing in Lithium-Ion Battery Cathode Active Materials. *J. Power Sources* **2020**, *466*, No. 228315.

(19) Bichon, M.; Sotta, D.; Dupré, N.; De Vito, E.; Boulineau, A.; Porcher, W.; Lestriez, B. Study of Immersion of $LiNi_{0.5}Mn_{0.3}Co_{0.2}O_2$ Material in Water for Aqueous Processing of Positive Electrode for Li-Ion Batteries. *ACS Appl. Mater. Interfaces* **2019**, *11*, 18331−18341.

(20) Hofmann, M.; Kapuschinski, M.; Guntow, U.; Giffin, G. A. Implications of Aqueous Processing for High Energy Density Cathode Materials: Part I. Ni-Rich Layered Oxides. *J. Electrochem. Soc.* **2020**, *167*, 140512.

(21) Loeffler, N.; Kim, G.-T.; Mueller, F.; Diemant, T.; Kim, J.-K.; Behm, R. J.; Passerini, S. In Situ Coating of $Li[Ni_{0.33}Mn_{0.33}Co_{0.33}]O_2$ Particles to Enable Aqueous Electrode Processing. *ChemSusChem* **2016**, *9*, 1112−1117.

(22) Kuenzel, M.; Bresser, D.; Diemant, T.; Carvalho, D. V.; Kim, G.-T.; Behm, R. J.; Passerini, S. Complementary Strategies Toward the Aqueous Processing of High-Voltage $LiNi_{0.5}Mn_{1.5}O_4$ Lithium-Ion Cathodes. *ChemSusChem* **2018**, *11*, 562−573.

(23) Kazzazi, A.; Bresser, D.; Birrozzi, A.; von Zamory, J.; Hekmatfar, M.; Passerini, S. Comparative Analysis of Aqueous Binders for High-Energy Li-Rich NMC as a Lithium-Ion Cathode and the Impact of Adding Phosphoric Acid. *ACS Appl. Mater. Interfaces* **2018**, *10*, 17214−17222.

(24) Xu, Y.; Mullaliu, A.; Lin, S. D.; Ma, Y.; Zarrabeitia, M.; Passerini, S.; Bresser, D. Effect of Phosphoric Acid as Slurry Additive on $Li_4Ti_5O_{12}$ Lithium-Ion Anodes. *Electrochim. Acta* **2022**, *429*, No. 140970.

(25) Lee, J.-H.; Lee, S.; Paik, U.; Choi, Y.-M. Aqueous Processing of Natural Graphite Particulates for Lithium-Ion Battery Anodes and

Their Electrochemical Performance. *J. Power Sources* **2005**, *147*, 249−255.
(26) Wu, Y.; Ben, L.; Yu, H.; Qi, W.; Zhan, Y.; Zhao, W.; Huang, X. Understanding the Effect of Atomic-Scale Surface Migration of Bridging Ions in Binding Li_3PO_4 to the Surface of Spinel Cathode Materials. *ACS Appl. Mater. Interfaces* **2019**, *11*, 6937−6947.
(27) Fleutot, B.; Davoisne, C.; Gachot, G.; Cavalaglio, S.; Grugeon, S.; Viallet, V. New Chemical Approach to Obtain Dense Layer Phosphate-Based Ionic Conductor Coating on Negative Electrode Material Surface: Synthesis Way, Outgassing and Improvement of C-Rate Capability. *Appl. Surf. Sci.* **2017**, *400*, 139−147.
(28) Li, X.; Yang, R.; Cheng, B.; Hao, Q.; Xu, H.; Yang, J.; Qian, Y. Enhanced Electrochemical Properties of Nano-Li_3PO_4 Coated on the $LiMn_2O_4$ Cathode Material for Lithium Ion Battery at 55 °C. *Mater. Lett.* **2012**, *66*, 168−171.
(29) Hofmann, M.; Nagler, F.; Kapuschinski, M.; Guntow, U.; Giffin, G. A. Surface Modification of $LiNi_{0.8}Co_{0.15}Al_{0.05}O_2$ Particles via Li_3PO_4 Coating to Enable Aqueous Electrode Processing. *ChemSusChem* **2020**, *13*, 5962−5971.
(30) Blyth, R. I. R.; Buqa, H.; Netzer, F. P.; Ramsey, M. G.; Besenhard, J. O.; Golob, P.; Winter, M. XPS Studies of Graphite Electrode Materials for Lithium Ion Batteries. *Appl. Surf. Sci.* **2000**, *167*, 99−106.
(31) Vogdanis, L.; Heitz, W. Carbon Dioxide as a Monomer, 3. The Polymerization of Ethylene Carbonate. *Makromol. Chem.* **1986**, *7*, 543−547.
(32) Gieu, J.-B.; Winkler, V.; Courrèges, C.; Ouatani, L. E.; Tessier, C.; Martinez, H. New Insights into the Characterization of the Electrode/Electrolyte Interfaces within $LiMn_2O_4/Li_4Ti_5O_{12}$ Cells, by X-Ray Photoelectron Spectroscopy, Scanning Auger Microscopy and Time-of-Flight Secondary Ion Mass Spectrometry. *J. Mater. Chem. A* **2017**, *5*, 15315−15325.
(33) Ehteshami, N.; Ibing, L.; Stolz, L.; Winter, M.; Paillard, E. Ethylene Carbonate-Free Electrolytes for Li-Ion Battery: Study of the Solid Electrolyte Interphases Formed on Graphite Anodes. *J. Power Sources* **2020**, *451*, No. 227804.
(34) Andersson, A. M.; Henningson, A.; Siegbahn, H.; Jansson, U.; Edström, K. Electrochemically Lithiated Graphite Characterised by Photoelectron Spectroscopy. *J. Power Sources* **2003**, *119*−*121*, 522−527.
(35) Song, M.-S.; Kim, R.-H.; Baek, S.-W.; Lee, K.-S.; Park, K.; Benayad, A. Is $Li_4Ti_5O_{12}$ a Solid-Electrolyte-Interphase-Free Electrode Material in Li-Ion Batteries? Reactivity between the $Li_4Ti_5O_{12}$ Electrode and Electrolyte. *J. Mater. Chem. A* **2014**, *2*, 631−636.
(36) Moulder, J. F. ; Stickle, W. F.; Sobol, P. E.; Bomben, K. D. *Handbook of X-Ray Photoelectron Spectroscopy: A Reference Book of Standard Spectra for Identification and Interpretation of XPS Data*; Physical Electronics Division, Perkin-Elmer Corporation, 1992; p 45.
(37) Biesinger, M. C.; Lau, L. W. M.; Gerson, A. R.; Smart, R. S. C. Resolving Surface Chemical States in XPS Analysis of First Row Transition Metals, Oxides and Hydroxides: Sc, Ti, V, Cu and Zn. *Appl. Surf. Sci.* **2010**, *257*, 887−898.
(38) Xu, Y.; Wan, L.; Liu, J.; Zeng, L.; Yang, Z. γ-Butyrolactone and Glutaronitrile as 5 V Electrolyte Additive and Its Electrochemical Performance for $LiNi_{0.5}Mn_{1.5}O_4$. *J. Alloys Compd.* **2017**, *698*, 207−214.
(39) Xu, Y.; Liu, J.; Zhou, L.; Zeng, L.; Yang, Z. FEC as the Additive of 5V Electrolyte and Its Electrochemical Performance for $LiNi_{0.5}Mn_{1.5}O_4$. *J. Electroanal. Chem.* **2017**, *791*, 109−116.
(40) Yang, G.; Shi, J.; Shen, C.; Wang, S.; Xia, L.; Hu, H.; Luo, H.; Xia, Y.; Liu, Z. Improving the Cyclability Performance of Lithium-Ion Batteries by Introducing Lithium Difluorophosphate ($LiPO_2F_2$) Additive. *RSC Adv.* **2017**, *7*, 26052−26059.